

Exploring Optimal Water Splitting Bifunctional Alloy Catalyst by Pareto Active Learning

Minki Kim, Yesol Kim, Min Young Ha, Euichul Shin, Seung Jae Kwak, Minhee Park, Il-Doo Kim, Woo-Bin Jung,* Won Bo Lee,* Yongjoo Kim,* and Hee-Tae Jung*

Design of bifunctional multimetallic alloy catalysts, which are one of the most promising candidates for water splitting, is a significant issue for the efficient production of renewable energy. Owing to large dimensions of the components and composition of multimetallic alloys, as well as the trade-off behavior in terms of the hydrogen evolution reaction (HER) and oxygen evolution reaction (OER) overpotentials for bifunctional catalysts, it is difficult to search for high-performance bifunctional catalysts with multimetallic alloys using conventional trial-and-error experiments. Here, an optimal bifunctional catalyst for water splitting is obtained by combining Pareto active learning and experiments, where 110 experimental data points out of 77946 possible points lead to effective model development. The as-obtained bifunctional catalysts for HER and OER exhibit high performance, which is revealed by model development using Pareto active learning; among the catalysts, an optimal catalyst ($\text{Pt}_{0.15}\text{Pd}_{0.30}\text{Ru}_{0.30}\text{Cu}_{0.25}$) exhibits a water splitting behavior of 1.56 V at a current density of 10 mA cm^{-2} . This study opens avenues for the efficient exploration of multimetallic alloys, which can be applied in multifunctional catalysts as well as in other applications.

reaction (OER)^[8–10] at the anode. Several studies have reported the improvement in the catalytic performance of each reaction; still a simplified system as well as improvement in the overall water splitting performance of a full cell have been continuously proposed.^[11,12] Moreover, the use of different catalysts for HER and OER can lead to cross-contamination of catalysts, thereby affecting the overall performance and stability of the reaction.^[13,14] Therefore, bifunctional catalysts, which can be applied for efficient HER and OER, are investigated. Among various materials, multimetallic alloys such as RuNiCo ,^[15] IrNiCu ,^[16] AlNiCoIrMo ,^[17] and CoFeLaNiPt ,^[18] have showed high performances. These multimetallic alloys have been investigated considerably in catalysis society due to several advantages. Compared to monometallic catalysts, multimetallic alloy catalysts demonstrate an unexpected behavior or a synergistic

effect.^[19] In addition, expensive noble metals can be substituted by cheaper non-noble metals while still exhibiting comparable performance.^[20,21] Meanwhile, few studies have determined the optimal content of bifunctional catalysts by tuning their components and composition.

For these reasons, finding an optimal balance between the participating reactions, and thus designing multimetallic alloys

1. Introduction

Water splitting has been attracting increasing attention owing to its possibility of substituting conventional fossil fuels and generating clean energy.^[1–4] The overall reaction for water splitting is categorized into two half-cell reactions: hydrogen evolution reaction (HER)^[5–7] at the cathode and the oxygen evolution

M. Kim, Y. Kim, H.-T. Jung
Department of Chemical and Biomolecular Engineering (BK21 four)
Korea Advanced Institute of Science and Technology (KAIST)
291 Daehak-ro, Yuseong-gu, Daejeon 34141, South Korea
E-mail: heetae@kaist.ac.kr


M. Kim, Y. Kim, H.-T. Jung
Korea Advanced Institute of Science and Technology (KAIST)
Institute for Nanocentury
Yuseong-gu, Daejeon 34141, South Korea

M. Y. Ha, S. J. Kwak, M. Park, W. B. Lee
School of Chemical and Biological Engineering
Institute of Chemical Processes
Seoul National University
Seoul 08826, South Korea
E-mail: wblee@snu.ac.kr

E. Shin, I.-D. Kim
Department of Materials Science and Engineering
Korea Advanced Institute of Science and Technology (KAIST)
291 Daehak-ro, Yuseong-gu, Daejeon 34141, South Korea

W.-B. Jung
John A. Paulson School of Engineering and Applied Sciences
Harvard University
Cambridge, MA 02138, USA
E-mail: woobinjung@seas.harvard.edu

Y. Kim
School of Advanced Materials Engineering
Kookmin University
Seoul 02707, South Korea
E-mail: cjyjee@kookmin.ac.kr

 The ORCID identification number(s) for the author(s) of this article can be found under <https://doi.org/10.1002/adma.202211497>.

DOI: 10.1002/adma.202211497

as a truly bifunctional catalyst is a daunting task. However, achieving the above goal solely by experiments is not feasible because of the enormous size of the design space, given the various components and compositions.^[22,23] Thus, to obtain a high performance bifunctional catalyst, it is crucial to efficiently search for all of the possible components and composition of the catalysts that can be fabricated. By conventional trial-and-error method, it is impossible to determine an optimal catalyst due to numerous possible combinations, which requires considerable time and cost. Another complexity in the search for an optimal bifunctional catalyst is that defining a single figure of merit to be optimized is difficult and arbitrary.^[24,25] A poorly designed figure of merit would lead to significant bias of the search process to a local subset of the design space, thereby hampering the general exploration of the design space. Hence, an ideal solution is to locate the Pareto front, where the set of Pareto-efficient solutions are not dominated by any other point; however, it is more difficult to accurately address the multidimensional search space considering the Pareto dominance relations.

Recent advances in computational techniques and the vast expansion of computing power could be utilized to screen candidates for their optimal composition and combination for bifunctional catalysts. Electronic calculation methods, e.g., density functional theory (DFT), have been extensively employed to calculate the adsorption energy of reactants on different catalytic surfaces,^[26–29] where scaling arguments have permitted the concise prediction of activities of different metallic catalysts. However, the computational costs associated with the high-throughput screening of bifunctional multimetallic alloy catalysts would easily increase on a formidable scale, especially when the mixture is composed of nontrivial fractions where the periodic unit cell used in DFT calculations should be substantially increased. Furthermore, the multimetallic alloy catalyst surface is decorated by graphene-like carbon atoms,^[30,31] where they directly affect the catalytic activities of the electronic structure which are difficult to calculate by conventional DFT methods. Although DFT calculation results clearly provide key insights into the activities of various surfaces of multimetallic alloy catalysts, it is difficult to extend the simulation results to the search of optimal compositions.

With respect to another aspect, computational methods can be utilized more directly to guide the trial-and-error search for an optimal composition of bifunctional catalysts. Instead of calculating the electronic structures by first-principle methods, black-box surrogate models that directly predict the catalytic activities from experimental process parameters,^[32–34] e.g., mole fraction of metallic precursors, can be designed. Especially, if the models can evaluate the uncertainties of predictions at given data points, the data points can be curated, where an experimental trial would result in the maximal gain of information: Such a machine-guided design of experiments is often called active learning.^[35–38] As can be demonstrated computationally and experimentally, a well-designed model using machine learning, especially active learning, can considerably reduce the number of evaluations, thereby greatly accelerating the search process.^[22,39–44]

Active learning is beneficial for several reasons. First, if the experimental evaluation is expensive or time-consuming, the potential reduction in the cost and time would considerably

surpass the additional effort of implementing an active learning framework. Second, if there are no theoretical or empirical relations to interpret the experimental behaviors, the black-box surrogate model can provide a robust interpolation of data. For all active learning models, searching for an optimal multimetallic component and composition for bifunctional catalysts is an ideal field to apply, and Pareto active learning, which is a multiobjective optimization method, is well-suited for this purpose. As the electrochemical evaluation of alloys with noble metals is both time-consuming and expensive, and currently, reliable models for the prediction of the bifunctional catalytic activity of multimetallic entropy alloys are not available, a new approach with Pareto active learning should be proposed.

In this study, a Pareto active learning framework and carbo-thermal shock (CTS) method were applied for nanoparticle synthesis to efficiently determine optimal metallic compositions for bifunctional catalysts of up to four component elements, which can be utilized for HER and OER. The Pareto active learning framework was built on two supervised learning models which are Gaussian process regressors (GPRs), which works on a large yet finite set of candidate compositions. At each iteration cycle, the models predicted the overpotential, evaluated the uncertainties of their own predictions, and suggested the composition to determine the next round of experiments that should be conducted. Guided by the two models, the uncertainty of the model for HER and OER overpotential values was decreased. In addition, the search trajectory revealed consistent improvements during the course of iterations, and the catalysts found within the iterations exhibited high catalytic properties, exhibiting a cell voltage of less than 1.6 V at a current density of 10 mA cm^{−2}. In addition, this approach can be applied to search multifunctional catalysts for use in reactions other than water splitting, which can help to optimize the catalytic activity toward different reactions. This approach can be extended even to searching multimetallic alloys for multifunctional applications, such as hydrogen storage, supercapacitors, and photocatalysts.^[45]

2. Results

2.1. Pareto Active Learning Model Construction

Figure 1a shows the overall workflow for exploring bifunctional multimetallic alloy catalysts for efficient water splitting. The workflow comprises two parts: 1) Experimental (synthesis, test, and analysis) part and 2) Pareto active learning part. In part (1) of the workflow, the catalysts were synthesized by the CTS method, and the catalysts were electrochemically tested to obtain overpotential data for the database that were used to develop the predictive model. In part (2) following part (1), based on the experimental data, two GPR models were trained to predict overpotentials for all possible combinations of metal elements for HER and OER, respectively. Then, each prediction point underwent a classification process to determine the points required from the experimental data. After classification, new data points were requested for experiments by providing information about the component and composition of the candidates, where the component and composition were based on the precursor solution. This process was repeated until a

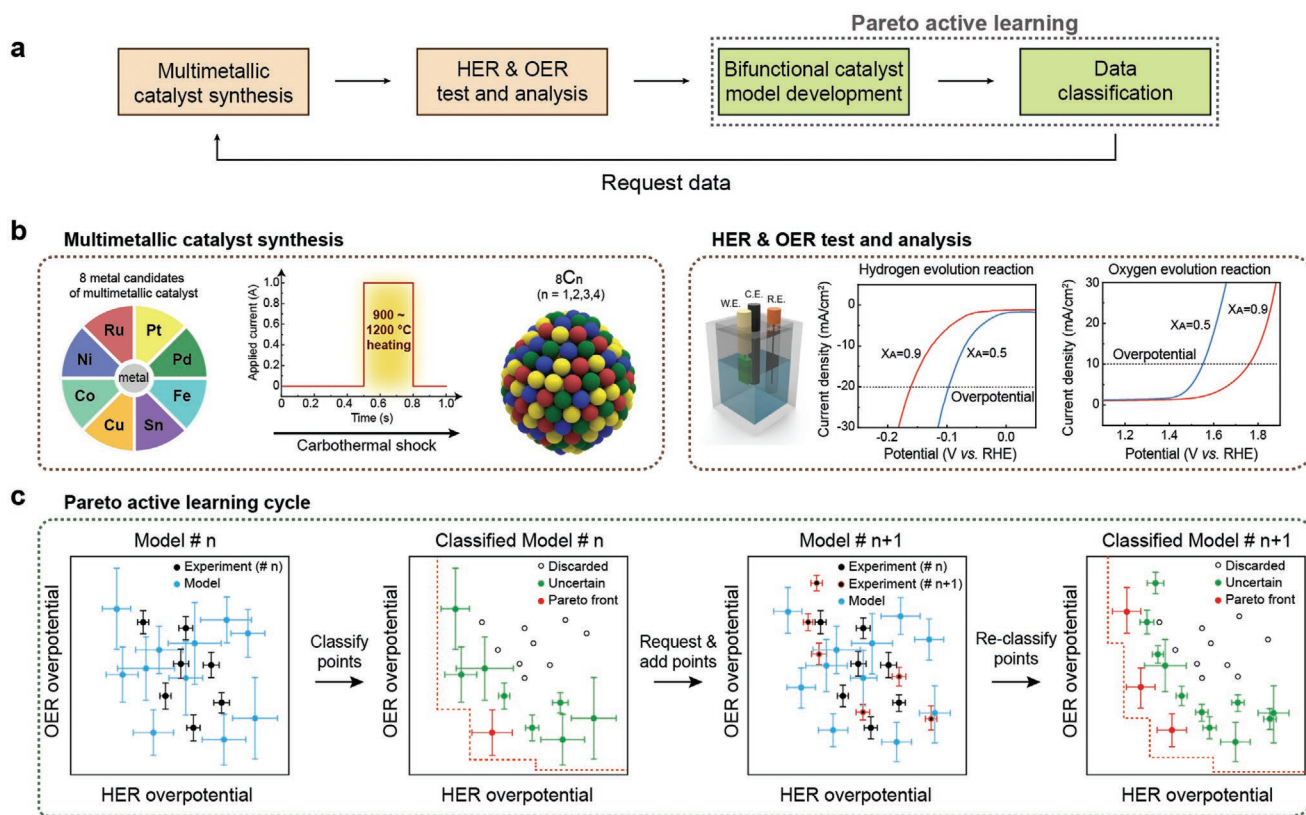


Figure 1. Overall workflow for the exploration of efficient bifunctional multimetallic alloy catalysts. a) Diagram showing the exploration of efficient bifunctional multimetallic alloy catalysts. b) Experimental part and c) Pareto active learning cycle part of exploring efficient bifunctional multimetallic alloy catalysts. Predicted data points are classified as discarded points, uncertain points, and Pareto front points. Discarded points are Pareto-dominated by another point. Uncertain points are points that require further measurements to be confirmed as either discarded points or Pareto front points. Pareto front points are points that are not dominated by other points.

significant fraction of the data space is classified as either “Pareto front” or “discarded;” in this work, we stopped the iteration when more than 75% of the data space was classified as “discarded.”

The detailed process of the experimental part comprised the synthesis of the multimetallic alloy catalyst by CTS and data collection after conducting electrochemical experiments (Figure 1b). Here, multimetallic alloy catalysts were fabricated by the CTS method, which is a rapid and simple method to prepare multimetallic alloy catalysts with few restrictions to metal selection. Nanoparticles in a randomly mixed state regardless of the metal elements were prepared by only drop casting a prepared metal precursor solution on the substrate and heating afterward.^[46] Thus, the CTS method is appropriate for the investigation of multimetallic alloy catalysts. In this study, eight elements, combination of noble and non-noble metals, were used as metal elements for multimetallic alloy catalyst: platinum (Pt),^[7] ruthenium (Ru),^[47] palladium (Pd),^[48] nickel (Ni),^[49] cobalt (Co),^[50,51] copper (Cu),^[6,52,53] tin (Sn),^[54,55] and iron (Fe),^[56,57] which are all known to exhibit activity toward water splitting reaction by forming alloy. After the combination of the elements from one to four ($8C_n$, $n = 1, 2, 3, 4$), a multimetallic alloy catalyst was synthesized as follows: preparing the carbon nanofiber (CNF) as the substrate, loading the metal precursor solution, conducting CTS by the application of a DC current to the substrate for Joule heating, and rapid cooling of the

substrate to form a multimetallic alloy catalyst. After the multimetallic alloy catalyst was synthesized, the substrate was cut and prepared for electrochemical experiments. Linear sweep voltammetry (LSV) was conducted from 0.05 to -0.50 V versus the reversible hydrogen electrode (RHE) for HER and from 0.91 to 2.01 V versus RHE for OER. Then, the overpotentials of HER and OER were measured, where the overpotential of HER was measured at 20 mA cm^{-2} , whereas the overpotential of OER was measured at 10 mA cm^{-2} . Even though 10 mA cm^{-2} is a conventional region to measure overpotential values, the overpotential of HER was measured at 20 mA cm^{-2} due to the usage of previous data done by this group.^[58]

After the measurements, overpotential values were utilized to develop a new model by Pareto active learning, which predicted the HER and OER overpotential values (Figure 1c). The predicted HER and OER overpotential values were designated as the x - and y -axes, respectively, and plotted in a 2D data space. A specific example scheme of plotting 2D data space from each of the overpotential data is shown in Figure S1 (Supporting Information). In addition, the model predicted the overpotentials for all the possible components and compositions of the catalyst, including experimental data points, as well as the uncertainty information. Then, all of the prediction points including experimental data points were classified to determine whether the prediction points belonged to three of the followings: discarded

point, uncertain point, and Pareto front point. If the data point was dominated by another point with confidence, it was classified as a discarded point, was omitted from the design space, and was not suggested for further experiments in the subsequent iteration. On the contrary, if the data point was not dominated by other points, it was classified as the Pareto front point. If there was no conformational certainty of whether the data point corresponded to any of the aforementioned points, it was classified as an uncertain point, requiring the classification by providing additional experimental data. These additional data included updating the same points or even updating the nearby points, because in active learning, other data points correlated to a particular data point also could affect the uncertainty of a certain data point. Thus, additional data for the model update were requested and added after the ongoing experimental procedure step. Again, the model was updated with a new prediction, and the prediction points were classified. By repeating this process, a model update of the bifunctional catalytic system is possible.

2.2. Initial Construction and Iteration of the Model

Figure 2 shows the initial construction of the model and its corresponding experimental results. First, the aforementioned interplay of Pareto active learning and experiments started with the initial information available to construct the initial model. Hence, the initial database for Pareto active learning is provided as an input to the model to obtain an initial prediction (Figure 2a). While constructing a model, it is better to have as many initial databases as possible to obtain a relatively accurate initial model. Previously, our group combined active learning and CTS experiments to search for a high-performance HER

catalyst.^[58] During the search of an optimal component and composition of a multimetallic alloy, 98 experimental data points were generated; the use of these data would be beneficial to the overall Pareto active learning process. By contrast, data for OER were not generated. Because it was necessary to have some initial data of OER for the development of the initial model, six random OER experimental data points were obtained, from unary to quaternary components.

Figure 2b shows the model development process from the initial model to the 1st model, where discarded points and uncertain points were represented by gray and orange, respectively. The initial database consisted of only six experimental data points for the OER overpotential; hence, marginal information is available on the structure of the data space. Furthermore, the initial database for OER was significantly biased, including only compositions derived mainly from a Pt–Ru–Ni ternary system with Fe and Sn added as the fourth element for a quaternary system; significant in-batch variation was only observed along the axes of Ru and Sn fractions (Table S1, Supporting Information). Note that the initial experimental data for OER were significantly biased, yielding length-scale parameters of the trained GPR model as low as 10^{-3} along the Ru and Sn axes and extremely high on all other axes. This result implies that the overpotential prediction of the model does not change under the variation of precursor fractions other than for Ru and Sn. From the limited training data, the model clustered the six data points into four clusters depending on the fraction of Ru and Sn, leading to four straight lines that are clustered with respect to the fractions of Ru and Sn precursors (left model of Figure 2b). On the other hand, the model provided a different prediction related to HER due to the larger amount of unbiased initial databases of HER compared with those of OER.

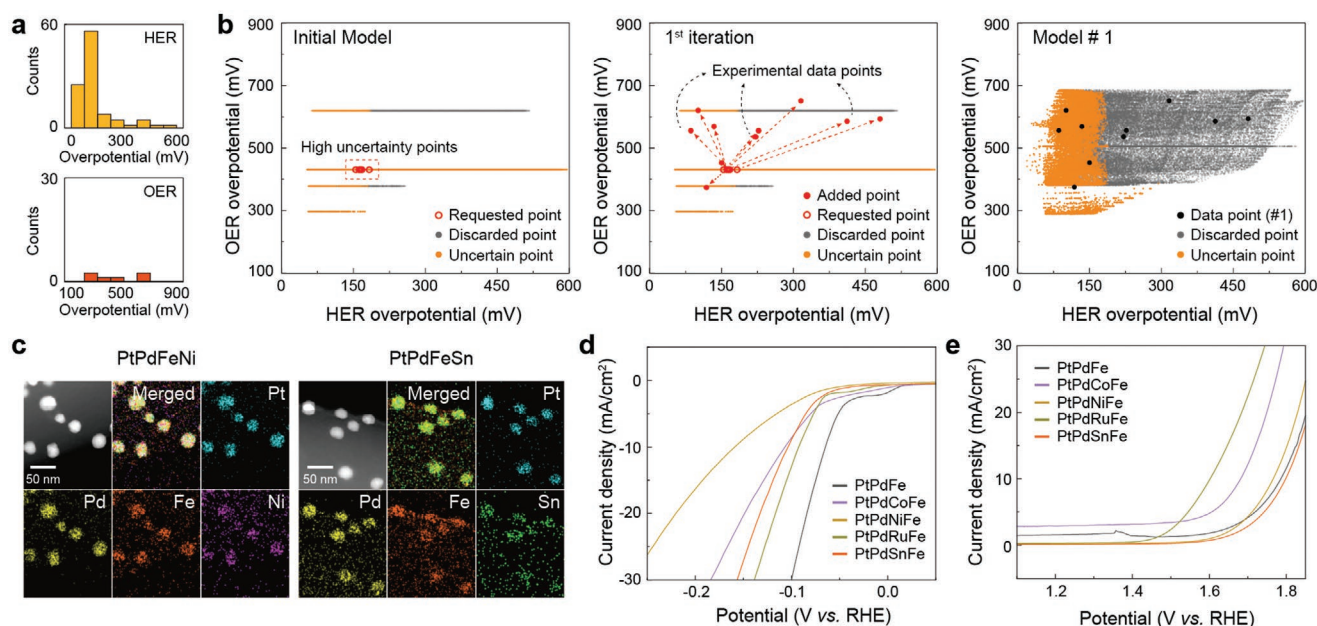


Figure 2. Construction of the initial model for Pareto active learning and its corresponding experimental results. a) Initial databases for HER and OER. Here, owing to the use of data from our previous study, the number of initial databases is biased to HER. b) Change in the initial model by adding data to the model. The model requests high uncertainty points, and by adding experimental data, which is requested by the model, a new model is updated by the classification of data into discarded and uncertain points. Here, discarded and uncertain points are colored as gray and orange, respectively. c) TEM–EDS images of PtPdFeNi and PtPdFeSn in the 1st iteration. LSV curves for d) HER and e) OER in the 1st iteration.

Then, all prediction points were classified, and the 10 highest uncertainty points were requested for subsequent experiments to develop the next model. The 1st iteration was conducted by obtaining 10 experimental values for predictions, and the model was updated drastically. As the developed model was at an early stage, a considerable difference between the prediction points and experimental data points was observed, evidenced by the red arrows in the middle graph of Figure 2b. After adding 10 experimental data to the model, a new model was developed, i.e., the 1st model, where both HER and OER predictions were scattered inside the 2D data space due to newly gained unbiased experimental data points related to OER. These data points were represented by black circles. The newly predicted model is shown in the right model of Figure 2b. The model distinguished between the discarded and uncertain points, where points with high HER and OER overpotential values were classified as discarded points, and points relatively near the axes were classified as uncertain points.

Figure 2c shows the transmission electron microscopy-energy-dispersive X-ray spectroscopy (TEM-EDS) image of the fabricated catalysts for the 1st iteration. Multimetallic nanoparticles were formed well by mixing, and the nanoparticles were relatively even, i.e., 26.7 nm for PtPdFeNi ($\text{Pt}_{0.15}\text{Pd}_{0.45}\text{Fe}_{0.20}\text{Ni}_{0.20}$) and 33.5 nm for PtPdFeSn ($\text{Pt}_{0.15}\text{Pd}_{0.45}\text{Fe}_{0.20}\text{Sn}_{0.20}$) (Figure S2, Supporting Information). In addition, the elements were well mixed, forming a random alloy. The merged image confirmed that the random alloy consists of every element used in the metal precursor solution. After synthesis, electrocatalytic measurements were conducted to determine the performance of the catalysts by LSV measurements. By controlling the precursor ratio of the catalyst, different overpotential values for HER and OER were obtained (Figure 2d,e). Among the experimental data points in the 1st iteration, PtPdFe ($\text{Pt}_{0.35}\text{Pd}_{0.40}\text{Fe}_{0.25}$) exhibited the best performance for HER, corresponding to an overpotential of

84.1 mV at a current density of 20 mA cm^{-2} , and PtPdRuFe ($\text{Pt}_{0.15}\text{Pd}_{0.45}\text{Ru}_{0.20}\text{Fe}_{0.20}$) exhibited the best performance for OER, corresponding to an overpotential of 373 mV at a current density of 10 mA cm^{-2} . The above procedures were repeated for subsequent feedback of the experimental steps and the model development steps to develop an accurate version of the model and to explore high-performance bifunctional catalysts.

2.3. Development of the Model with Iteration

By adding experimental data points suggested by the model, some changes to the model prediction were observed with the progress of iteration. Figure 3 shows a specific process of the Pareto active learning procedure from the 4th model to the 5th model. First, the 4th model was developed by the addition of 30 more experimental data points from the 1st model (Figure 3a). Here, black circles inside the model represented data points obtained by experiment from the 1st iteration through the 4th iteration. Compared to the 1st model in Figure 2b, the discarded points in the 4th model were clustered more on the upper right side, where the catalysts were expected to exhibit poor performance. Furthermore, the vacant space in the 1st model in the bottom left side for the OER overpotential was filled with predicted data points due to the additional update of experimental data points. After the classification of the predicted data points, the requested data points, which should be obtained by experiments from the next iteration, were represented as red hollow circles, exhibiting the highest uncertainty among points classified as uncertain points. These requested data points were synthesized with the given precursor component and composition, and their HER and OER overpotentials were updated by electrochemically testing and analysis (Figure 3b), and these experimental data points were represented

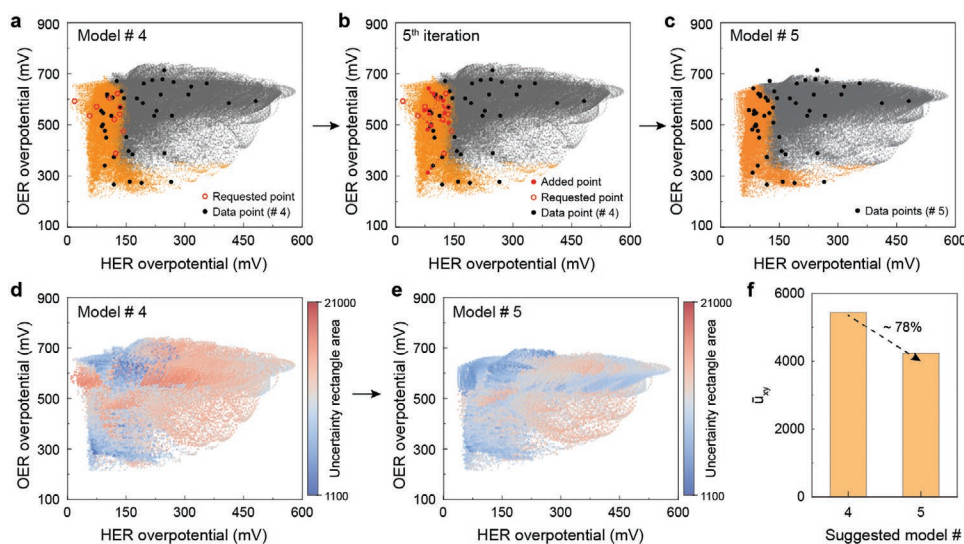


Figure 3. Procedure of Pareto active learning in the 5th iteration and its corresponding model. a) Prediction of the 4th model with experimental data (black circles). b) Ten points with the largest uncertainty rectangle area (red hollow circles) were sorted and suggested for experimental evaluations. Measured HER and OER overpotentials at the suggested compositions were updated into the database with the results (red filled circles). c) The model was retrained to update the predictions in the data space to obtain the 5th model. d) The 4th model and e) 5th model with uncertainty information, respectively. The scale bars are in log scale, and the units of the numbers in the scale bar are mV^2 . f) Value of the average uncertainty rectangle for the 4th model and 5th model. After 5th iteration, the average uncertainty rectangle decreased to $\approx 78\%$ of the uncertainty of the 4th model.

as red filled circles. Then, the next model (5th model) was developed with the added experimental data points from the 5th iteration and classified (Figure 3c). Although only 10 experimental data were added to the 4th model, the prediction in the 5th model was changed, completely affecting the entire data space.

To compare the accuracy of the model before and after the 5th iteration, an uncertainty rectangle area (u_{xy}), which was defined as the multiplied value for each axes ($u_{xy} = u_x \times u_y$), was also depicted in the data space by the application of color to the data points, as can be seen in Figure 3d,e. Here, high uncertainty of the data points is represented as red, whereas low uncertainty of the data points is represented as blue. Compared to the 4th model where a majority of red dots were observed, the 5th model exhibited a considerably lower uncertainty, with blue dots dominating the data space. Notably, not only the color of the updated data points or their surrounding parts changed but also the uncertainty decreased for the regions where no additional data points were added in the 5th iteration. This is because the updated data points have affected points with similar component and composition. Adding data points also affected points that exhibited high uncertainty in the discarded point region, thus decreasing the overall uncertainty of the model. Thus, after the 5th iteration, the average uncertainty rectangle area (\bar{u}_{xy}) decreased to $\approx 78\%$ of the value of the previous model (Figure 3f). By only adding 10 experimental data which showed the highest uncertainty in the uncertain point region, the overall uncertainty of the model significantly decreased.

It should be noted that GPR models are in principle not able to extrapolate in the data space. However, since the design space is restricted to the hyperplane in an 8D space of compositions, it is intrinsically bounded and can be explicitly enumerated. When provided with a sufficiently dense training data in the design space, the problem is essentially an interpolation problem to deduce overpotential of an unseen point from the data of the measured points. In the early stage of the active learning loops, the training data are sparsely distributed and the model prediction does not show statistically better performance than random sampling. However, as training data accumulate in the later stage of learning, the model acquires dense enough data points performing reliable interpolations from nearby measurements, where the model suggestion turns out to be relevant for the search of Pareto-optimal points.

2.4. Final Developed Model after Pareto Active Learning Iterations

After 6 more cycles of Pareto active learning from the 5th model, a meaningful plateau in the number of points classified as discarded points was observed. After 11 iterations from the initial database, where 110 experimental points were added out of 77946 prediction points, the Pareto active learning procedure was terminated, and the result was analyzed (Figure 4). First, all of the models were depicted, as shown in Figure 4a and Figure S3

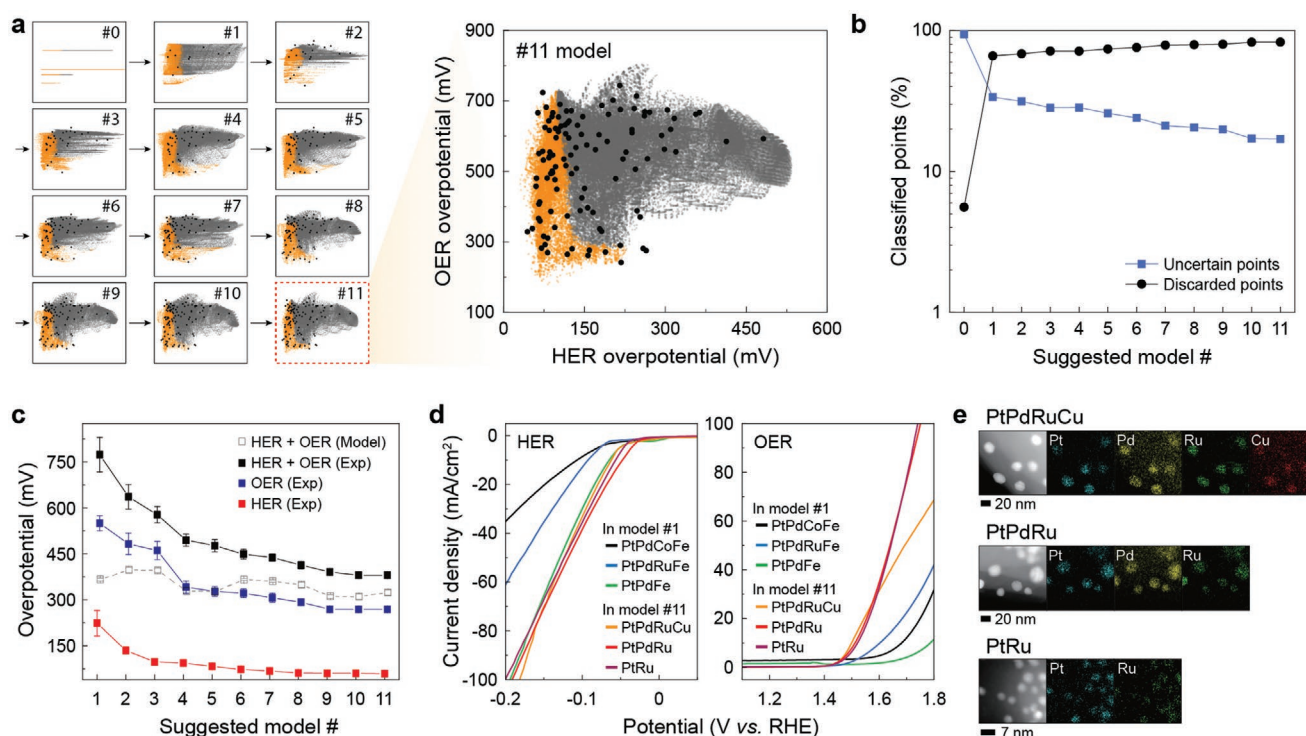


Figure 4. Final result of the Pareto active learning and characterization of the catalyst. a) Result of the Pareto active learning model for each step and the corresponding data points. The 11th model, which is the final model developed in this study, is plotted with HER and OER overpotential axes. b) Uncertain ratio of the model according to model number. c) Averaged overpotential values of the lowest top 10 accumulated data points after each iteration for HER, OER, and summation of the overpotential values. Lowest top 10 values suggested by the model are also plotted. d) LSV curve of HER and OER for the top three catalysts discovered in the 1st model and the 11th model. e) TEM-EDS images of the top three catalysts discovered in this study, which are PtPdRuCu, PtPdRu, and PtRu, respectively.

(Supporting Information), and the final model (11th model) was plotted with overpotential values. From the initial model to the 7th model, the shape of the model changed substantially as 10 experimental data points were added to the model. In particular, in the early stages of the model, only a few number of discarded points were located in the bottom part, specifically on the right part. However, with the progress of iteration, some of the top left part and bottom right part were also classified as discarded points. Finally, in the 11th model, the upper part and right part were classified as discarded points. In addition, compared with that observed in the 7th model, the discarded points were more concentrated in the upper right part, and the cluster of the uncertain points formed an L-shape.

This tendency was also observed in Figure 4b, where the points classified as uncertain points decreased to $\approx 15\%$ of the whole prediction points (77946 points by setting the grid spacing as 0.05), and the discarded points increased with the progress of iteration, indicating that Pareto active learning is well directed to classify discarded points among all data points. Then, the averaged overpotential values of the lowest top 10 accumulated data points after each iteration were identified to determine whether our methodology was successful in searching for high-performance catalysts with the update of each model. As can be observed in Figure 4c, for all overpotential values including HER, OER, and the summation values of HER and OER, a plateau was observed only after 11 iterations, indicative of successful and effective Pareto active learning. Then, the lowest top 10 values suggested by the model were also plotted and compared with the experimental results. In the early stages of the model, uncertainty values were extremely high, resulting in a large deviation of the lowest top 10 values between the model and experimental results. However, with the progress of Pareto active learning, this gap started to decrease, and when learning was terminated, overpotential values for the lowest top 10 experimental data were comparable to the prediction values of the model, verifying the increased accuracy of the model.

2.5. Characterization for Synthesized Bifunctional Water Splitting Catalysts

Among the 110 experimental points inside the data space, the LSV of the top three points for the 1st model and the 11th model are shown in Figure 4d to confirm whether the model is successfully guided to find better catalysts. The component and composition of the top three points for the 1st model were PtPdFe ($\text{Pt}_{0.35}\text{Pd}_{0.40}\text{Fe}_{0.25}$), PtPdCoFe ($\text{Pt}_{0.15}\text{Pd}_{0.45}\text{Co}_{0.20}\text{Fe}_{0.20}$), PtPdRuFe ($\text{Pt}_{0.15}\text{Pd}_{0.45}\text{Ru}_{0.20}\text{Fe}_{0.20}$), respectively, whereas the top three points for the 11th model were PtPdRuCu ($\text{Pt}_{0.15}\text{Pd}_{0.30}\text{Ru}_{0.30}\text{Cu}_{0.25}$), PtPdRu ($\text{Pt}_{0.15}\text{Pd}_{0.20}\text{Ru}_{0.65}$), and PtRu ($\text{Pt}_{0.40}\text{Ru}_{0.60}$), respectively, in which the precursor composition was informed as brackets. HER overpotential values for the 1st model were 116.7, 148.7, and 84.1 mV, whereas the HER overpotential values for the 11th model were 79.8, 68.6, and 75.1 mV. These different catalytic activities were also verified by the different Tafel slopes shown in Figure S4 (Supporting Information). The different HER catalytic activities among these top three points in the 11th model compared to the 1st model were also verified by the charge-transfer resistance (R_{ct}) value in the Nyquist plot, which was measured by

electrochemical impedance spectroscopy (EIS) analysis (Figure S5, Supporting Information): PtPdRu exhibited the smallest diameter of the semicircle in the Nyquist plot for HER, indicative of small R_{ct} , and the samples from the 11th model had smaller diameter of the semicircle compared to the samples from the 1st model. In addition, as Figure 4c shows, OER overpotential values were greater than HER overpotential values for high-performance catalysts; hence, the tendency of the summation of overpotential values was similar to the OER overpotential values. The OER overpotential values for top three points in the 1st model were 373, 452, and 556 mV, respectively, whereas the top three points in the 11th model were 268, 287, and 291 mV, respectively. The R_{ct} of the top three points at the OER active voltage (1.6 V vs RHE) supported the increasing order of the overpotential values of PtPdRuCu ($4.2 \Omega \text{ cm}^{-2}$), PtPdRu ($6.8 \Omega \text{ cm}^{-2}$), and PtRu ($8.7 \Omega \text{ cm}^{-2}$), also following the order of OER catalytic performance.

To investigate the component and composition of the synthesized multimetallic alloy catalysts and to confirm their entropy alloy structure, the top three bifunctional catalysts in the 11th model were analyzed by scanning electron microscopy (SEM), TEM, and TEM-EDS (Figure 4e and Figure S6 (Supporting Information)). TEM and TEM-EDS images revealed that the multimetallic nanoparticles were fabricated on CNF under a particle size of 20 nm with each of the components mixed well. From TEM-EDS analysis, compositions of each catalyst were $\text{Pt}_{0.215}\text{Pd}_{0.208}\text{Ru}_{0.420}\text{Cu}_{0.157}$, $\text{Pt}_{0.153}\text{Pd}_{0.313}\text{Ru}_{0.524}$, and $\text{Pt}_{0.365}\text{Ru}_{0.635}$ (Figure S7, Supporting Information). In addition, the corresponding compositions of the same catalysts by X-ray photoelectron spectroscopy (XPS) analysis were $\text{Pt}_{0.175}\text{Pd}_{0.412}\text{Ru}_{0.313}\text{Cu}_{0.100}$, $\text{Pt}_{0.144}\text{Pd}_{0.274}\text{Ru}_{0.582}$, and $\text{Pt}_{0.358}\text{Ru}_{0.642}$. As reported in previous literatures, the precursor ratio and the ratio of synthesized nanoparticles were slightly different due to different physical properties such as vapor pressure and transition temperatures.^[46] Compared to XPS spectra before heating where the metal ion peaks corresponded to the main chemical states of the metal, the metallic states are the main chemical states after heating, indicating successful fabrication by CTS (Figures S8–S11, Supporting Information).

By 11 iterations along with the model development, the saturation of the model uncertainty as well as the performance of the water splitting behavior was observed. It was possible to search for catalysts with a satisfactory water splitting performance, in which the added overpotential values for HER and OER were less than 1.6 V at a current density of 10 mA cm^{-2} with negligible decrease in performance after 10 h of reaction (Figure S12, Supporting Information). Specifically, PtPdRuCu, PtPdRu, and PtRu were the top three catalysts discovered herein, exhibiting superior catalytic performances compared with those of the catalysts found in the early models. This iterative feedback process between Pareto active learning and experiments made it possible to search for high-performance catalysts more efficiently in comparison to the currently used trial-and-error method or computational techniques.

3. Conclusion

In this study, high-performance bifunctional catalysts for water splitting were determined by the iterative feedback process of

Pareto active learning and experiments. By utilizing the initial database with the obtained experimental data and developing the model, it was possible to progress the development of the model into a more accurate manner using a small amount of data. Compared to the early stages of model, the final model exhibited considerably lower number of uncertain points as well as higher catalytic activities for HER and OER. Within this process, it was possible to find several catalysts that exhibited excellent catalytic performance compared with those tested in the initial step of the model. Therefore, by appropriate model construction with a small amount of experimental data, high-performance catalysts can be discovered using this system. This model construction is not limited to bifunctional catalysts for water splitting, indicating that it can be expanded to different catalytic reaction fields or even other multifunctional applications. A possible direction of further research would be introducing problem-specific learning models to enhance the performance of the prediction models in the active learning loop, either by feature engineering, kernel optimization, or increasing the complexity of the models.

4. Experimental Section

Fabrication of a CNF Substrate: Polyacrylonitrile (PAN) ink solution was formed by dissolving PAN in *N,N*-dimethylformamide and stirring at room temperature. After overnight stirring, electrospinning was conducted using stirred PAN ink solution, where the solution was put in a syringe with a metal nozzle and voltage was applied between the collector and the metal nozzle. The collector was wrapped in silicone-coated paper foil, leading to facile detachment of PAN NF. After electrospinning process, the attached freestanding PAN NF membrane was gently detached from the collector. CNF substrate was fabricated through a 1 h stabilization in air and 2 h carbonization in argon condition on PAN NFs. Details of the fabrication of CNF substrate could be seen in the previous work.^[58]

Preparation of the Precursor Solution: All chemicals were purchased from Sigma-Aldrich. The precursor chemicals were as follows: chloroplatinic(IV) acid hydrate, ruthenium(III) chloride hydrate, palladium(II) chloride, cobalt(II) chloride, nickel(II) chloride, copper(II) chloride, iron(III) chloride hexahydrate, and tin(II) chloride. The above precursors were mixed with ethanol at the concentration of 0.1 M to make precursor solutions.

Fabrication of the Alloy Nanoparticles: The prepared substrates (CNF) were attached to the quartz by applying silver paste to the copper tape. Then, 200 μ L of the prepared precursor solutions in volume with different ratios according to the experimental conditions were dropped on the substrate while heating at 80 $^{\circ}$ C. After ethanol was fully evaporated, carbothermal shock method (300 ms heating under Ar) was applied to synthesize multimetallic nanoparticles.

HER and OER Test in Single Cell: Electrochemical test of the fabricated electrodes was done by using a potentiostat (Biologic VSP). Three electrodes were used inside the cell: a working electrode, a reference electrode (Ag/AgCl in 3 M NaCl), and a counter electrode (carbon rod). For the electrolyte, H₂SO₄ solution with concentration of 0.5 M (45 mL, pH \approx 0.3) was used, and magnetic stirring was done during the reaction. The calculated potential was automatically IR-corrected by the function in the potentiostat. Cyclic voltammetry was conducted at a scan rate of 5 mV s⁻¹ from 0.05 to -0.5 V versus RHE for HER, and was conducted from 0.909 to 2.009 V versus RHE with the same scan rate for OER. EIS was performed at -0.2 and 1.6 V versus RHE with frequency range from 0.01 to 100 kHz.

Characterization: To observe the morphology of the alloy nanoparticles on CNF, SEM (Hitachi, SU5000) and TEM (Talos F200X) were employed. High-angle annular dark-field scanning transmission electron

microscopy was used in the bright field mode to confirm the fabricated alloy nanoparticles and energy-dispersive X-ray spectrometry of TEM was used to confirm the component and composition of elements in alloy particles. The component and composition of elements were also confirmed by XPS (Thermo Scientific, Nexsa G2).

GPR: To predict the overpotential and suggest an optimal search trajectory in a multimetallic composition space, two GPRs were adopted as the learning agents in the active learning scheme, where each regressor learnt the overpotential for HER and OER, respectively. The input to the models was 8D composition vectors, where the dimensions denoted the mole fraction of Pt, Pd, Ru, Ni, Fe, Cu, Co, and Sn precursors before the CTS. The output of the two models was the overpotential for HER and OER, which was measured as described in the Experimental Section.

The GPR models used squared-exponential covariance kernels augmented with a white noise kernel

$$k(x, x') = \sigma_s^2 \exp\left(-\frac{\|x - x'\|^2}{2l^2}\right) + \sigma_n^2 \delta(x - x') \quad (1)$$

In the first term, σ_s and l denote the signal level and length scale, respectively, where l was also an 8D vector. Elements of l were the length scale of the variation of overpotential along that direction: for example, in case of small l_{Pt} , the overpotential varied greatly with the change in the fraction of Pt precursor, and vice versa. The second term denoted the noise level of the experimental measurement itself: if the second term was omitted from the kernel, the model suffered from overfitting to the training data.

A trained GPR model yielded the mean and standard deviation at a provided query point. The mean was the prediction for the overpotential at a given composition, and the standard deviation was understood as the uncertainty of the prediction. Hence, the model obtained a considerable amount of information by performing additional experiments on compositions with large uncertainties.

In the 2D space of the HER and OER overpotentials, each data point was associated with the uncertainty rectangle, whose area was defined as the product of the standard deviations from the HER and OER models. The lower and upper boundaries of the uncertainty rectangle corresponded to the optimistic and pessimistic estimates of the overpotential, respectively.

ϵ -Pareto Front: In addition to the uncertainty estimation by GPR models, the data space was further reduced by ruling out the points that were predicted to be inferior in terms of the catalytic performances. As two objective functions were present, i.e., the overpotentials of HER and OER, the two data points were compared by a Pareto dominance relation: point x dominated point x' if the HER and OER overpotentials of x were less than those of x' . In this study, the objective was to locate the Pareto front or the set of points that were not dominated by any other point.

As the overpotentials of HEA catalysts were continuous functions of the precursor compositions, it was impossible to determine a finite number of noise-free points in the Pareto front. Hence, it was practically important to define a method to discretize the data space, where a small difference in the overpotential was neglected for the efficiency of the search process. This was conducted by defining the ϵ -Pareto dominance relation:^[59–61] if the pessimistic estimates of HER and OER of a point x were less than the optimistic estimates of a point x' , then x' was ϵ -dominated by x .

ϵ -Pareto Active Learning Iterations: Active learning iterations were performed as follows. First, using the available overpotential data, two GPR models were trained to predict the overpotentials of HER and OER for all points in the composition space. Second, based on the uncertainty hyperrectangles, the points were classified into three categories: Pareto front, discarded, and uncertain. Third, among the uncertain points, ten compositions with the largest uncertainty hyperrectangles were suggested for future experiments. Finally, the HER and OER overpotentials were measured at the suggested points, and the GPR models were retrained with the measured experimental data.

This procedure was repeated until the points with sufficient catalytic performances for HER and OER were located. Complete details of the GPR models and ε -Pareto active learning procedure are provided in the Supporting Information.

Supporting Information

Supporting Information is available from the Wiley Online Library or from the author.

Acknowledgements

M.K., Y.K., and M.Y.H. contributed equally to this work. This research was funded by the Saudi Aramco-KAIST CO₂ Management Center, Electronics and Telecommunications Research Institute (ETRI) grant funded by the Korean government (Grant No. 22ZB1200), and the National Research Foundation (NRF) of the Korean Government through the Ministry of Science, ICT, and Future Planning (MSIP) (Grant Nos. NRF2021K1A4A8A01079356, NRF2021M3H4A6A01041234).

Conflict of Interest

The authors declare no conflict of interest.

Data Availability Statement

The data that support the findings of this study are available from the corresponding author upon reasonable request.

Keywords

bifunctional catalyst, machine learning, multimetallic alloy, Pareto active learning, water splitting

Received: December 8, 2022

Revised: February 3, 2023

Published online: March 18, 2023

- [1] X. Li, X. Hao, A. Abudula, G. Guan, *J. Mater. Chem. A* **2016**, 4, 11973.
- [2] L.-W. Chen, H.-W. Liang, *Catal. Sci. Technol.* **2021**, 11, 4673.
- [3] B. Sachin Kumar, K. Tarafder, A. R. Shetty, A. C. Hegde, V. C. Gudla, R. Ambat, S. K. Kalpathy, S. Anandhan, *Dalton Trans.* **2019**, 48, 12684.
- [4] X. Li, L. Zhao, J. Yu, X. Zhang, H. Liu, W. Zhou, *Nano-Micro Lett.* **2020**, 12, 131.
- [5] E. J. Popczun, J. R. McKone, C. G. Read, A. J. Biacchi, A. M. Wiltrout, N. S. Lewis, R. E. Schaak, *J. Am. Chem. Soc.* **2013**, 135, 9267.
- [6] W. Xu, S. Zhu, Y. Liang, Z. Cui, X. Yang, A. Inoue, H. Wang, *J. Mater. Chem. A* **2017**, 5, 18793.
- [7] K. Li, Y. Li, Y. Wang, J. Ge, C. Liu, W. Xing, *Energy Environ. Sci.* **2018**, 11, 1232.
- [8] S. Chen, J. Duan, M. Jaroniec, S. Z. Qiao, *Adv. Mater.* **2014**, 26, 2925.
- [9] H.-J. Qiu, G. Fang, J. Gao, Y. Wen, J. Lv, H. Li, G. Xie, X. Liu, S. Sun, *ACS Mater. Lett.* **2019**, 1, 526.
- [10] Z. P. Wu, H. Zhang, S. Zuo, Y. Wang, S. L. Zhang, J. Zhang, S. Q. Zang, X. W. D. Lou, *Adv. Mater.* **2021**, 33, 2103004.
- [11] H. Li, F. Ke, J. Zhu, *Nanomaterials* **2018**, 8, 89.
- [12] R. Bose, V. R. Jothi, K. Karuppasamy, A. Alfantazi, S. C. Yi, *J. Mater. Chem. A* **2020**, 8, 13795.
- [13] J. Li, Y. Wang, T. Zhou, H. Zhang, X. Sun, J. Tang, L. Zhang, A. M. Al-Enizi, Z. Yang, G. Zheng, *J. Am. Chem. Soc.* **2015**, 137, 14305.
- [14] W. Luo, Y. Wang, L. Luo, S. Gong, Y. Li, X. Gan, *Appl. Surf. Sci.* **2022**, 606, 154808.
- [15] Y. Xue, Q. Yan, X. Bai, Y. Xu, X. Zhang, Y. Li, K. Zhu, K. Ye, J. Yan, D. Cao, G. Wang, *J. Colloid Interface Sci.* **2022**, 612, 710.
- [16] J. Zhang, Z. Chen, C. Liu, J. Zhao, S. Liu, D. Rao, A. Nie, Y. Chen, Y. Deng, W. Hu, *Sci. China Mater.* **2019**, 63, 249.
- [17] Z. Jin, J. Lv, H. Jia, W. Liu, H. Li, Z. Chen, X. Lin, G. Xie, X. Liu, S. Sun, H. J. Qiu, *Small* **2019**, 15, e1904180.
- [18] M. W. Glasscott, A. D. Pendergast, S. Goines, A. R. Bishop, A. T. Hoang, C. Renault, J. E. Dick, *Nat. Commun.* **2019**, 10, 2650.
- [19] B. X. Cao, C. Wang, T. Yang, C. T. Liu, *Scr. Mater.* **2020**, 187, 250.
- [20] Y. Yan, B. Y. Xia, B. Zhao, X. Wang, *J. Mater. Chem. A* **2016**, 4, 17587.
- [21] N. K. Oh, J. Seo, S. Lee, H. J. Kim, U. Kim, J. Lee, Y. K. Han, H. Park, *Nat. Commun.* **2021**, 12, 4606.
- [22] K. Tran, Z. W. Ulissi, *Nat. Catal.* **2018**, 1, 696.
- [23] J. Noh, S. Back, J. Kim, Y. Jung, *Chem. Sci.* **2018**, 9, 5152.
- [24] Y. Gorlin, T. F. Jaramillo, *J. Am. Chem. Soc.* **2010**, 132, 13612.
- [25] J. A. Vigil, T. N. Lambert, B. T. Christensen, *J. Mater. Chem. A* **2016**, 4, 7549.
- [26] J. R. Kitchin, *Nat. Catal.* **2018**, 1, 230.
- [27] B. R. Goldsmith, J. Esterhuizen, J. X. Liu, C. J. Bartel, C. Sutton, *AIChE J.* **2018**, 64, 2311.
- [28] S. Back, K. Tran, Z. W. Ulissi, *ACS Catal.* **2019**, 9, 7651.
- [29] A. J. Chowdhury, W. Yang, E. Walker, O. Mamun, A. Heyden, G. A. Terejanu, *J. Phys. Chem. C* **2018**, 122, 28142.
- [30] Z. Huang, Y. Yao, Z. Pang, Y. Yuan, T. Li, K. He, X. Hu, J. Cheng, W. Yao, Y. Liu, A. Nie, S. Sharifi-Asl, M. Cheng, B. Song, K. Amine, J. Lu, T. Li, L. Hu, R. Shahbazian-Yassar, *Nat. Commun.* **2020**, 11, 6373.
- [31] W. B. Jung, H. Park, J. S. Jang, D. Y. Kim, D. W. Kim, E. Lim, J. Y. Kim, S. Choi, J. Suk, Y. Kang, I. D. Kim, J. Kim, M. Wu, H. T. Jung, *ACS Nano* **2021**, 15, 4235.
- [32] J. E. Gubernatis, T. Lookman, *Phys. Rev. Mater.* **2018**, 2, 120301.
- [33] R. Yuan, Z. Liu, P. V. Balachandran, D. Xue, Y. Zhou, X. Ding, J. Sun, D. Xue, T. Lookman, *Adv. Mater.* **2018**, 30, 1702884.
- [34] P. Raccuglia, K. C. Elbert, P. D. Adler, C. Falk, M. B. Wenny, A. Molloy, M. Zeller, S. A. Friedler, J. Schrier, A. J. Norquist, *Nature* **2016**, 533, 73.
- [35] B. Settles, *Active Learning: Synthesis Lectures on Artificial Intelligence and Machine Learning*, Morgan & Claypool Publishers, San Rafael, CA, USA **2012**.
- [36] S. Langner, F. Häse, J. D. Perea, T. Stubhan, J. Hauch, L. M. Roch, T. Heumüller, A. Aspuru-Guzik, C. J. Brabec, *Adv. Mater.* **2020**, 32, 1907801.
- [37] F. Häse, L. M. Roch, T. Heumüller, C. Kreisbeck, A. Aspuru-Guzik, *ACS Cent. Sci.* **2018**, 4, 1134.
- [38] T. Lookman, P. V. Balachandran, D. Xue, R. Yuan, *npj Comput. Mater.* **2019**, 5, 21.
- [39] R. A. Flores, C. Paolucci, K. T. Winther, A. Jain, J. A. G. Torres, M. Aykol, J. Montoya, J. K. Nørskov, M. Bajdich, T. Bligaard, *Chem. Mater.* **2020**, 32, 5854.
- [40] H. A. Doan, G. Agarwal, H. Qian, M. J. Counihan, J. Rodríguez-López, J. S. Moore, R. S. Assary, *Chem. Mater.* **2020**, 32, 6338.
- [41] W. Wang, T. Yang, W. H. Harris, R. Gomez-Bombarelli, *Chem. Commun.* **2020**, 56, 8920.
- [42] K. Gubaev, E. V. Podryabinkin, G. L. W. Hart, A. V. Shapeev, *Comput. Mater. Sci.* **2019**, 156, 148.
- [43] M. Zhong, K. Tran, Y. Min, C. Wang, Z. Wang, C.-T. Dinh, P. D. Luna, Z. Yu, A. S. Rasouli, P. Brodersen, S. Sun, O. Voznyy, C.-S. Tan,

- M. Askerka, F. Che, M. Liu, A. Seifitokaldani, Y. Pang, S.-C. Lo, A. Ip, Z. Ulissi, E. H. Sargent, *Nature* **2020**, 581, 178.
- [44] L. Chen, Y. Tian, X. Hu, S. Yao, Z. Lu, S. Chen, X. Zhang, Z. Zhou, *Adv. Funct. Mater.* **2022**, 32, 2208418.
- [45] Y. Ma, Y. Ma, Q. Wang, S. Schweidler, M. Botros, T. Fu, H. Hahn, T. Brezesinski, B. Breitung, *Energy Environ. Sci.* **2021**, 14, 2883.
- [46] Y. Yao, Z. Huang, P. Xie, S. D. Lacey, R. J. Jacob, H. Xie, F. Chen, A. Nie, T. Pu, M. Rehboldt, D. Yu, M. R. Zachariah, C. Wang, R. Shahbazian-Yassar, J. Li, L. Hu, *Science* **2018**, 359, 1489.
- [47] B. S. Yeo, *Nat. Catal.* **2019**, 2, 284.
- [48] A. Barhoum, H. H. El-Maghrabi, A. A. Nada, S. Sayegh, S. Roualdes, A. Renard, I. Iatsunskyi, E. Coy, M. Bechelany, *J. Mater. Chem. A* **2021**, 9, 17724.
- [49] F. Chen, Y. Yao, A. Nie, S. Xu, J. Dai, E. Hitz, Y. Li, A. Lu, Z. Huang, T. Li, R. Shahbazian-Yassar, L. Hu, *Adv. Energy Mater.* **2018**, 8, 1800466.
- [50] H. Liang, C. Yang, S. Ji, N. Jiang, X. An, X. Yang, H. Wang, R. Wang, *Catal. Commun.* **2019**, 124, 1.
- [51] L. K. Wu, W. Y. Wu, J. Xia, H. Z. Cao, G. Y. Hou, Y. P. Tang, G. Q. Zheng, *J. Mater. Chem. A* **2017**, 5, 10669.
- [52] T. Chao, X. Luo, W. Chen, B. Jiang, J. Ge, Y. Lin, G. Wu, X. Wang, Y. Hu, Z. Zhuang, Y. Wu, X. Hong, Y. Li, *Angew. Chem., Int. Ed.* **2017**, 56, 16047.
- [53] X. Cao, E. Johnson, M. Nath, *J. Mater. Chem. A* **2019**, 7, 9877.
- [54] L. Lang, Y. Shi, J. Wang, F. B. Wang, X. H. Xia, *ACS Appl. Mater. Interfaces* **2015**, 7, 9098.
- [55] Q. Zhang, H. Qi, C. Hou, N. Liu, J. Guan, *Mater. Today Energy* **2019**, 14, 100364.
- [56] F. McKay, Y. Fang, O. Kizilkaya, P. Singh, D. D. Johnson, A. Roy, D. P. Young, P. T. Sprunger, J. C. Flake, W. A. Shelton, Y. Xu, *J. Phys. Chem. C* **2021**, 125, 17008.
- [57] H. Liu, M. Zha, Z. Liu, J. Tian, G. Hu, L. Feng, *Chem. Commun.* **2020**, 56, 7889.
- [58] M. Kim, M. Y. Ha, W. B. Jung, J. Yoon, E. Shin, I. D. Kim, W. B. Lee, Y. Kim, H. T. Jung, *Adv. Mater.* **2022**, 34, 2108900.
- [59] M. Zuluaga, A. Krause, M. Püschel, *J. Mach. Learn. Res.* **2016**, 17, 1.
- [60] K. M. Jablonka, G. M. Jothiappan, S. Wang, B. Smit, B. Yoo, *Nat. Commun.* **2021**, 12, 2312.
- [61] G. Agarwal, H. A. Doan, L. A. Robertson, L. Zhang, R. S. Assary, *Chem. Mater.* **2021**, 33, 8133.